

hep-ph/0412054
 UMN-TH-2332/04
 FTPI-MINN-04/45
 December 2004

Dark Matter Candidates in Supersymmetric Models¹

Keith A. Olive

William I. Fine Theoretical Physics Institute,
 University of Minnesota, Minneapolis, MN 55455, USA olive@umn.edu

¹To be published in “Dark 2004”, proceedings of 5th International Heidelberg Conference on Dark Matter in Astro and Particle Physics, eds. H.V. Klapdor-Kleingrothaus and R. Arnowitt.

The status of the constrained minimal supersymmetric standard model (CMSSM) will be discussed in light of our current understanding of the relic density after WMAP. A global likelihood analysis of the model is performed including data from direct Higgs searches, global fits to electroweak data, $b \rightarrow s\gamma$, the anomalous magnetic moment of the muon, as well as the cosmological relic density. Also considered are models which relax and further constrain the CMSSM. Prospects for dark matter detection in colliders and cryogenic detectors will be briefly discussed.

1 Introduction

Supersymmetric models with conserved R -parity contain one new stable particle which is a candidate for cold dark matter (CDM) [1]. There are very strong constraints, however, forbidding the existence of stable or long lived particles which are not color and electrically neutral. The sneutrino [2] is one possible candidate, but in the MSSM, it has been excluded as a dark matter candidate by direct [3] and indirect [4] searches. Another possibility is the gravitino and is probably the most difficult to exclude. This possibility has been discussed recently in the CMSSM context [6]. I will concentrate on the remaining possibility in the MSSM, namely the neutralinos.

There are four neutralinos, each of which is a linear combination of the $R = -1$, neutral fermions [1]: the wino \tilde{W}^3 , the partner of the 3rd component of the $SU(2)_L$ gauge boson; the bino, \tilde{B} , the partner of the $U(1)_Y$ gauge boson; and the two neutral Higgsinos, \tilde{H}_1 and \tilde{H}_2 . In general, the neutralino mass eigenstates can be expressed as a linear combination

$$\chi = \alpha \tilde{B} + \beta \tilde{W}^3 + \gamma \tilde{H}_1 + \delta \tilde{H}_2 \quad (1)$$

The solution for the coefficients α, β, γ and δ for neutralinos that make up the LSP can be found by diagonalizing the mass matrix which depends on $M_1(M_2)$ which are the soft supersymmetry breaking $U(1)$ ($SU(2)$) gaugino mass terms, μ , the supersymmetric Higgs mixing mass parameter and the

two Higgs vacuum expectation values, v_1 and v_2 . One combination of these is related to the Z mass, and therefore is not a free parameter, while the other combination, the ratio of the two vevs, $\tan \beta$, is free.

The most general version of the MSSM, despite its minimality in particles and interactions contains well over a hundred new parameters. The study of such a model would be untenable were it not for some (well motivated) assumptions. These have to do with the parameters associated with supersymmetry breaking. It is often assumed that, at some unification scale, all of the gaugino masses receive a common mass, $m_{1/2}$. The gaugino masses at the weak scale are determined by running a set of renormalization group equations. Similarly, one often assumes that all scalars receive a common mass, m_0 , at the GUT scale. These too are run down to the weak scale. The remaining supersymmetry breaking parameters are the trilinear mass terms, A_0 , which I will also assume are unified at the GUT scale, and the bilinear mass term B . There are, in addition, two physical CP violating phases which will not be considered here.

The natural boundary conditions at the GUT scale for the MSSM would include μ and B in addition to $m_{1/2}$, m_0 , and A_0 . In this case, upon running the RGEs down to a low energy scale and minimizing the Higgs potential, one would predict the values of M_Z , $\tan \beta$ (in addition to all of the sparticle masses). Since M_Z is known, it is more useful to analyze supersymmetric models where M_Z is input rather than output. It is also common to treat $\tan \beta$ as an input parameter. This can be done at the expense of shifting μ (up to a sign) and B from inputs to outputs. This model is often referred to as the constrained MSSM or CMSSM. Once these parameters are set, the entire spectrum of sparticle masses at the weak scale can be calculated. In the CMSSM, the solutions for μ generally lead to a neutralino which which very nearly a pure \tilde{B} .

2 The CMSSM after WMAP

For a given value of $\tan \beta$, A_0 , and $sgn(\mu)$, the resulting regions of acceptable relic density and which satisfy the phenomenological constraints can be displayed on the $m_{1/2} - m_0$ plane. In Fig. 1a, the light shaded region corresponds to that portion of the CMSSM plane with $\tan \beta = 10$, $A_0 = 0$, and $\mu > 0$ such that the computed relic density yields $0.1 < \Omega_\chi h^2 < 0.3$. At relatively low values of $m_{1/2}$ and m_0 , there is a large ‘bulk’ region which tapers off as $m_{1/2}$ is increased. At higher values of m_0 , annihilation cross sections are too small to maintain an acceptable relic density and $\Omega_\chi h^2 > 0.3$. Although sfermion masses are also enhanced at large $m_{1/2}$ (due to RGE running), co-annihilation processes between the LSP and the next lightest sparticle (in this case the $\tilde{\tau}_1$) enhance the annihilation cross section and reduce the relic density. This occurs when the LSP and NLSP are nearly degenerate in mass.

The dark shaded region has $m_{\tilde{\tau}_1} < m_\chi$ and is excluded. Neglecting coannihilations, one would find an upper bound of ~ 450 GeV on $m_{1/2}$, corresponding to an upper bound of roughly 200 GeV on m_B . The effect of coannihilations is to create an allowed band about 25-50 GeV wide in m_0 for $m_{1/2} \lesssim 1400$ GeV, which tracks above the $m_{\tilde{\tau}_1} = m_\chi$ contour [5].

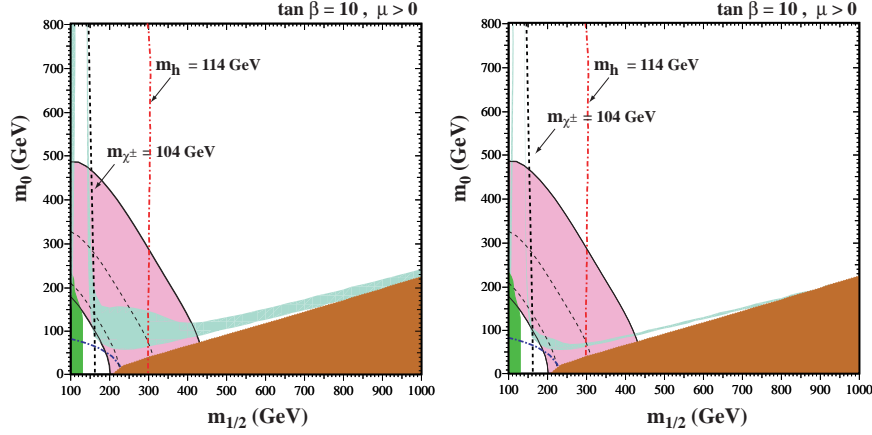


Fig. 1. The $(m_{1/2}, m_0)$ planes for (a) $\tan \beta = 10$ and $\mu > 0$, assuming $A_0 = 0$, $m_t = 175$ GeV and $m_b(m_b)_{SM}^{MS} = 4.25$ GeV. The near-vertical (red) dot-dashed lines are the contours $m_h = 114$ GeV, and the near-vertical (black) dashed line is the contour $m_{\chi^\pm} = 104$ GeV. Also shown by the dot-dashed curve in the lower left is the corner excluded by the LEP bound of $m_{\tilde{e}} > 99$ GeV. The medium (dark green) shaded region is excluded by $b \rightarrow s\gamma$, and the light (turquoise) shaded area is the cosmologically preferred regions with $0.1 \leq \Omega_\chi h^2 \leq 0.3$. In the dark (brick red) shaded region, the LSP is the charged $\tilde{\tau}_1$. The region allowed by the E821 measurement of a_μ at the 2σ level, is shaded (pink) and bounded by solid black lines, with dashed lines indicating the 1σ ranges. In (b), the relic density is restricted to the range $0.094 < \Omega_\chi h^2 < 0.129$.

Also shown in Fig. 1a are the relevant phenomenological constraints. These include the limit on the chargino mass: $m_{\chi^\pm} > 104$ GeV [7], on the selectron mass: $m_{\tilde{e}} > 99$ GeV [8] and on the Higgs mass: $m_h > 114$ GeV [9]. The former two constrain $m_{1/2}$ and m_0 directly via the sparticle masses, and the latter indirectly via the sensitivity of radiative corrections to the Higgs mass to the sparticle masses, principally $m_{\tilde{t}, \tilde{b}}$. FeynHiggs [10] is used for the calculation of m_h . The Higgs limit imposes important constraints principally on $m_{1/2}$ particularly at low $\tan \beta$. Another constraint is the requirement that the branching ratio for $b \rightarrow s\gamma$ is consistent with the experimental measurements [11]. These measurements agree with the Standard Model, and therefore provide bounds on MSSM particles [12, 13], such as the chargino and charged Higgs masses, in particular. Typically, the $b \rightarrow s\gamma$ constraint

is more important for $\mu < 0$, but it is also relevant for $\mu > 0$, particularly when $\tan \beta$ is large. The constraint imposed by measurements of $b \rightarrow s\gamma$ also excludes small values of $m_{1/2}$. Finally, there are regions of the $(m_{1/2}, m_0)$ plane that are favoured by the BNL measurement [14] of $g_\mu - 2$ at the 2σ level, corresponding to a deviation from the Standard Model calculation [15] using e^+e^- data. One should be however aware that this constraint is still under active discussion.

The preferred range of the relic LSP density has been altered significantly by the recent improved determination of the allowable range of the cold dark matter density obtained by combining WMAP and other cosmological data: $0.094 < \Omega_{CDM} < 0.129$ at the 2σ level [16]. In the second panel of Fig. 1, we see the effect of imposing the WMAP range on the neutralino density [17, 18, 19]. We see immediately that (i) the cosmological regions are generally much narrower, and (ii) the ‘bulk’ regions at small $m_{1/2}$ and m_0 have almost disappeared, in particular when the laboratory constraints are imposed. Looking more closely at the coannihilation regions, we see that (iii) they are significantly truncated as well as becoming much narrower, since the reduced upper bound on $\Omega_\chi h^2$ moves the tip where $m_\chi = m_{\tilde{\tau}}$ to smaller $m_{1/2}$ so that the upper limit is now $m_{1/2} \lesssim 950$ GeV or $m_\chi \lesssim 400$ GeV.

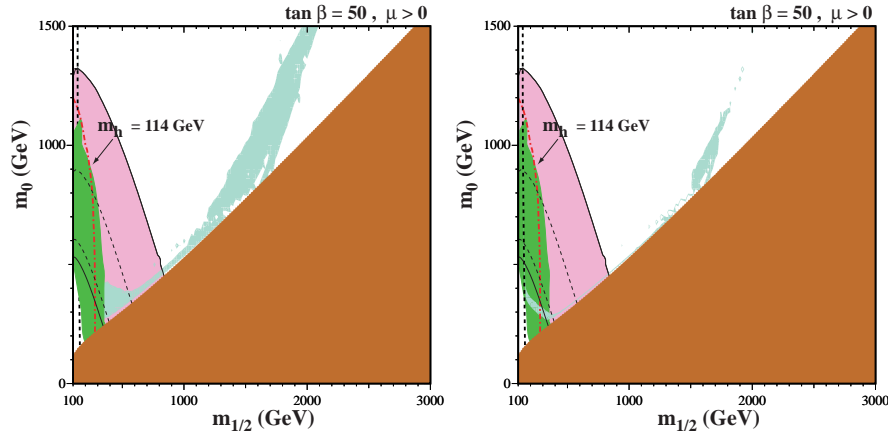


Fig. 2. As in Fig. 1 for $\tan \beta = 50$.

Another mechanism for extending the allowed CMSSM region to large m_χ is rapid annihilation via a direct-channel pole when $m_\chi \sim \frac{1}{2}m_A$ [20, 21]. Since the heavy scalar and pseudoscalar Higgs masses decrease as $\tan \beta$ increases, eventually $2m_\chi \simeq m_A$ yielding a ‘funnel’ extending to large $m_{1/2}$ and m_0 at large $\tan \beta$, as seen in the high $\tan \beta$ strips of Fig. 2. As one can see, the impact of the Higgs mass constraint is reduced (relative to the case with $\tan \beta = 10$) while that of $b \rightarrow s\gamma$ is enhanced.

Shown in Fig. 3 are the WMAP lines [17] of the $(m_{1/2}, m_0)$ plane allowed by the new cosmological constraint $0.094 < \Omega_\chi h^2 < 0.129$ and the laboratory constraints listed above, for $\mu > 0$ and values of $\tan \beta$ from 5 to 55, in steps $\Delta(\tan \beta) = 5$. We notice immediately that the strips are considerably narrower than the spacing between them, though any intermediate point in the $(m_{1/2}, m_0)$ plane would be compatible with some intermediate value of $\tan \beta$. The right (left) ends of the strips correspond to the maximal (minimal) allowed values of $m_{1/2}$ and hence m_χ . The lower bounds on $m_{1/2}$ are due to the Higgs mass constraint for $\tan \beta \leq 23$, but are determined by the $b \rightarrow s\gamma$ constraint for higher values of $\tan \beta$.

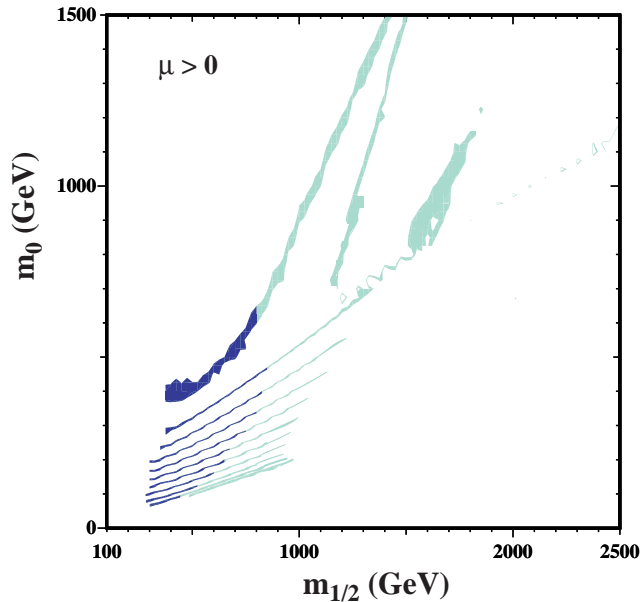


Fig. 3. The strips display the regions of the $(m_{1/2}, m_0)$ plane that are compatible with $0.094 < \Omega_\chi h^2 < 0.129$ and the laboratory constraints for $\mu > 0$ and $\tan \beta = 5, 10, 15, 20, 25, 30, 35, 40, 45, 50, 55$. The parts of the strips compatible with $g_\mu - 2$ at the 2σ level have darker shading.

Finally, there is one additional region of acceptable relic density known as the focus-point region [22], which is found at very high values of m_0 . An example showing this region is found in Fig. 4, plotted for $\tan \beta = 10$, $\mu > 0$, and $m_t = 175$ TeV. As m_0 is increased, the solution for μ at low energies as determined by the electroweak symmetry breaking conditions eventually begins to drop. When $\mu \lesssim m_{1/2}$, the composition of the LSP gains a strong Higgsino component and as such the relic density begins to drop precipitously.

These effects are both shown in Fig. 5 where the value of μ and Ωh^2 are plotted as a function of m_0 for fixed $m_{1/2} = 300$ GeV and $\tan \beta = 10$. As m_0 is increased further, there are no longer any solutions for μ . This occurs in the shaded region in the upper left corner of Fig. 4.

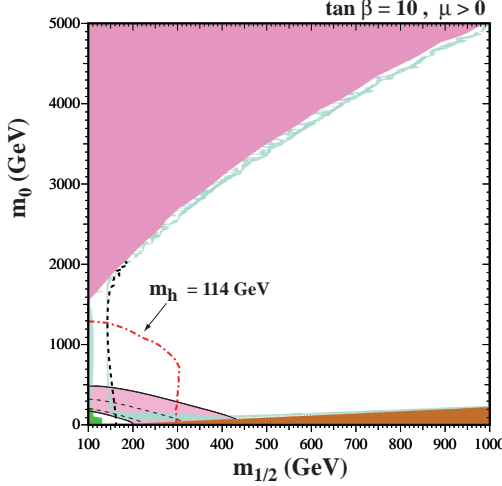


Fig. 4. As in Fig. 1a, where the range in m_0 is extended to 5 TeV. In the shaded region at very high m_0 , there are no solutions for μ which respect the low energy electroweak symmetry breaking conditions.

Fig. 5 also exemplifies the degree of fine tuning associated with the focus-point region. While the position of the focus-point region in the $m_0, m_{1/2}$ plane is not overly sensitive to supersymmetric parameters, it is highly sensitive to the top quark Yukawa coupling which contributes to the evolution of μ [23, 24]. As one can see in the figure, a change in m_t of 3 GeV produces a shift of about 2.5 TeV in m_0 . Note that the position of the focus-point region is also highly sensitive to the value of A_0/m_0 . In Fig. 5, $A_0 = 0$ was chosen. For $A_0/m_0 = 0.5$, the focus point shifts from 2.5 to 4.5 TeV and moves to larger m_0 as A_0/m_0 is increased.

3 A Likelihood analysis of the CMSSM

Up to now, in displaying acceptable regions of cosmological density in the $m_0, m_{1/2}$ plane, it has been assumed that the input parameters are known with perfect accuracy so that the relic density can be calculated precisely. While all of the beyond the standard model parameters are completely unknown and therefore carry no formal uncertainties, standard model parame-

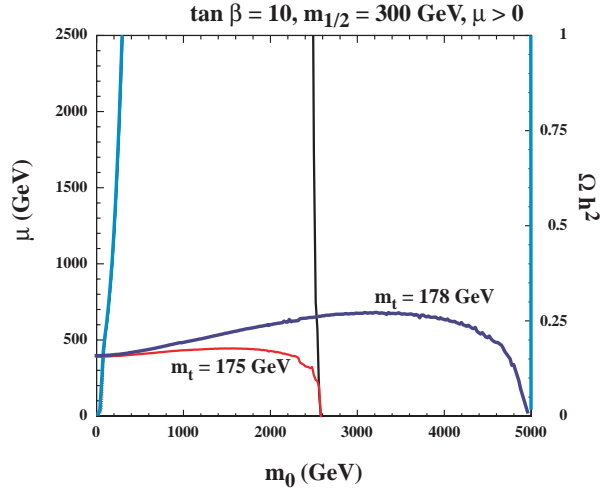


Fig. 5. The value of μ as a function of m_0 for fixed $m_{1/2} = 300$ GeV and $\tan \beta = 10$ for two choices of m_t as indicated. The scale on the right gives the value of Ωh^2 . The curves corresponding to this is scale rise sharply at low m_0 to values much larger than 1. For $m_t = 175$ GeV and $m_0 \approx 2500$ GeV, the value of Ωh^2 drops to acceptable values when μ becomes small. When the $m_t = 178$ GeV, Ωh^2 drops at $m_0 \approx 5000$ GeV.

ters such as the top and bottom Yukawa couplings are known but do carry significant uncertainties. Indeed, we saw that in the case of the focus-point region, there is an intense sensitivity of the relic density to the top quark Yukawa. Other regions in the $m_0, m_{1/2}$ plane, such as those corresponding to the rapid annihilation funnels are also very sensitive to the 3rd generation Yukawas.

The optimal way to combine the various constraints (both phenomenological and cosmological) is via a likelihood analysis, as has been done by some authors both before [25] and after [18] the WMAP data was released. When performing such an analysis, in addition to the formal experimental errors, it is also essential to take into account theoretical errors, which introduce systematic uncertainties that are frequently non-negligible. Recently, we have performed an extensive likelihood analysis of the CMSSM [26]. Included is the full likelihood function for the LEP Higgs search, as released by the LEP Higgs Working Group. This includes the small enhancement in the likelihood just beyond the formal limit due to the LEP Higgs signal reported late in 2000. This was re-evaluated most recently in [9], and cannot be regarded as significant evidence for a light Higgs boson. We have also taken into account the indirect information on m_h provided by a global fit to the precision electroweak data. The likelihood function from this indirect source does not vary

rapidly over the range of Higgs masses found in the CMSSM, but we included this contribution with the aim of completeness.

The interpretation of the combined Higgs likelihood, \mathcal{L}_{exp} , in the $(m_{1/2}, m_0)$ plane depends on uncertainties in the theoretical calculation of m_h . These include the experimental error in m_t and (particularly at large $\tan \beta$) m_b , and theoretical uncertainties associated with higher-order corrections to m_h . Our default assumptions are that $m_t = 175 \pm 5$ GeV for the pole mass, and $m_b = 4.25 \pm 0.25$ GeV for the running \overline{MS} mass evaluated at m_b itself. The theoretical uncertainty in m_h , σ_{th} , is dominated by the experimental uncertainties in $m_{t,b}$, which are treated as uncorrelated Gaussian errors:

$$\sigma_{th}^2 = \left(\frac{\partial m_h}{\partial m_t} \right)^2 \Delta m_t^2 + \left(\frac{\partial m_h}{\partial m_b} \right)^2 \Delta m_b^2. \quad (2)$$

Typically, we find that $(\partial m_h / \partial m_t) \sim 0.5$, so that σ_{th} is roughly 2-3 GeV.

The combined experimental likelihood, \mathcal{L}_{exp} , from direct searches at LEP 2 and a global electroweak fit is then convolved with a theoretical likelihood (taken as a Gaussian) with uncertainty given by σ_{th} from (2) above. Thus, we define the total Higgs likelihood function, \mathcal{L}_h , as

$$\mathcal{L}_h(m_h) = \frac{\mathcal{N}}{\sqrt{2\pi} \sigma_{th}} \int dm'_h \mathcal{L}_{exp}(m'_h) e^{-(m'_h - m_h)^2 / 2\sigma_{th}^2}, \quad (3)$$

where \mathcal{N} is a factor that normalizes the experimental likelihood distribution.

In addition to the Higgs likelihood function, we have included the likelihood function based on $b \rightarrow s\gamma$. The branching ratio for these decays has been measured by the CLEO, BELLE and BaBar collaborations [11], and we took as the combined value $\mathcal{B}(b \rightarrow s\gamma) = (3.54 \pm 0.41 \pm 0.26) \times 10^{-4}$. The theoretical prediction [12, 13] contains uncertainties which stem from the uncertainties in m_b , α_s , the measurement of the semileptonic branching ratio of the B meson as well as the effect of the scale dependence. While the likelihood function based on the measurements of the anomalous magnetic moment of the muon was considered in [26], it will not be discussed here.

Finally, in calculating the likelihood of the CDM density, we take into account the contribution of the uncertainties in $m_{t,b}$. We will see that the theoretical uncertainty plays a very significant role in this analysis. The likelihood for Ωh^2 is therefore,

$$\mathcal{L}_{\Omega h^2} = \frac{1}{\sqrt{2\pi} \sigma} e^{-(\Omega h^{2th} - \Omega h^{2exp})^2 / 2\sigma^2}, \quad (4)$$

where $\sigma^2 = \sigma_{exp}^2 + \sigma_{th}^2$, with σ_{exp} taken from the WMAP [16] result and σ_{th}^2 from (2), replacing m_h by Ωh^2 .

The total likelihood function is computed by combining all the components described above:

$$\mathcal{L}_{tot} = \mathcal{L}_h \times \mathcal{L}_{bs\gamma} \times \mathcal{L}_{\Omega h^2} (\times \mathcal{L}_{a_\mu}) \quad (5)$$

The likelihood function in the CMSSM can be considered a function of two variables, $\mathcal{L}_{tot}(m_{1/2}, m_0)$, where $m_{1/2}$ and m_0 are the unified GUT-scale gaugino and scalar masses respectively. Results are based on a Bayesian analysis, in which a prior range for $m_{1/2}$ is introduced in order to normalize the conditional probability obtained from the likelihood function using Bayes' theorem. Although it is possible to motivate some upper limit on $m_{1/2}$, e.g., on the basis of naturalness [27, 24, 28], one cannot quantify any such limit rigorously. Within the selected range, we adopt a flat prior distribution for $m_{1/2}$, and normalize the volume integral:

$$\int \mathcal{L}_{tot} dm_0 dm_{1/2} = 1 \quad (6)$$

for each value of $\tan \beta$, combining where appropriate both signs of μ . We note that no such prior need be specified for m_0 . For any given value of $m_{1/2}$, the theory is well defined only up to some maximum value of m_0 , above which radiative electroweak symmetry breaking is no longer possible. We always integrate up to that point, adopting also a flat prior distribution for m_0 .

In Fig. 6 the likelihood along slices through the CMSSM parameter space for $\tan \beta = 10$, $A_0 = 0$, $\mu > 0$, and $m_{1/2} = 300$ and 800 GeV is shown in the left and right panels, respectively, plotting the likelihood as a function of m_0 . The solid red curves show the total likelihood function calculated including the uncertainties which stem from the experimental errors in m_t and m_b . The peak at low m_0 is due to the coannihilation region. The peak at $m_0 \simeq 2500(4500)$ GeV for $m_{1/2} = 300(800)$ GeV is due to the focus-point region. Also shown in Fig. 6 are the 68%, 90%, and 95% CL (horizontal) lines, corresponding to the iso-likelihood values of the fully integrated likelihood function corresponding to the solid (red) curve.

The focus-point peak is suppressed relative to the coannihilation peak at low m_0 because of the theoretical sensitivity to the experimental uncertainty in the top mass. We recall that the likelihood function is proportional to σ^{-1} , and that σ which scales with $\partial(\Omega_\chi h^2)/\partial m_t$, is very large at large m_0 [24]. The error due to the uncertainty in m_t is far greater in the focus-point region than in the coannihilation region. Thus, even though the exponential in $\mathcal{L}_{\Omega_\chi h^2}$ is of order unity near the focus-point region when $\Omega_\chi h^2 \simeq 0.1$, the prefactor is very small due the large uncertainty in the top mass. This accounts for the factor of $\gtrsim 1000$ suppression seen in Fig. 6 when comparing the two peaks of the solid red curves.

We note also that there is another broad, low-lying peak at intermediate values of m_0 . This is due to a combination of the effects of σ in the prefactor and the exponential. We expect a bump to occur when the Gaussian exponential is of order unity, i.e., $\Omega_\chi h^2 \sim \sqrt{2} \Delta m_t \partial \Omega_\chi h^2 / \partial m_t$. $\Omega_\chi h^2 \sim 10$ at large m_0 for our nominal value $m_t = 175$ GeV, but it varies significantly as one samples the favoured range of m_t within its present uncertainty. The competition between the exponential and the prefactor would require a large theoretical uncertainty in $\Omega_\chi h^2$: $\partial \Omega_\chi h^2 / \partial m_t \sim 2$ for $\Delta m_t = 5$ GeV. This

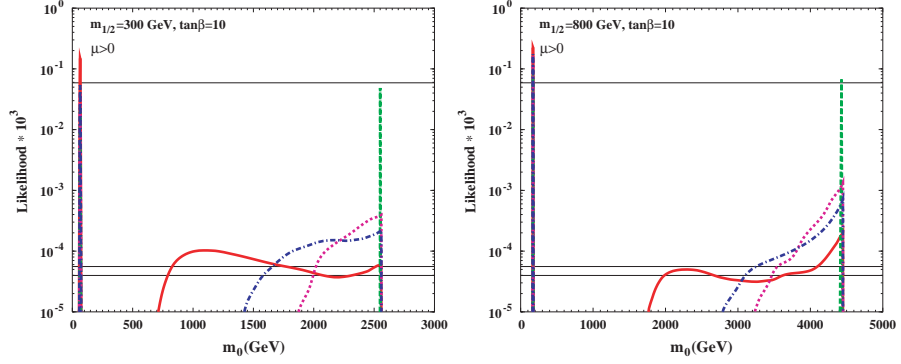


Fig. 6. The likelihood function along slices in m_0 through the CMSSM parameter space for $\tan\beta = 10$, $A_0 = 0$, $\mu > 0$ and $m_{1/2} = 300, 800$ GeV in the left and right panels, respectively. The red (solid) curves are calculated using the current errors in m_t and m_b , the green dashed curve with no error in m_t , the violet dotted lines with $\Delta m_t = 0.5$ GeV, and the blue dashed-dotted lines with $\Delta m_t = 1$ GeV.

occurs when $m_0 \sim 1000$ GeV, which is the position of the broad secondary peak in Fig. 6a. At higher m_0 , σ continues to grow, and the prefactor suppresses the likelihood function until $\Omega_\chi h^2$ drops to ~ 0.1 in the focus-point region.

As is clear from the above discussion, the impact of the present experimental error in m_t is particularly important in this region. This point is further demonstrated by the differences between the curves in each panel, where we decrease *ad hoc* the experimental uncertainty in m_t . As Δm_t is decreased, the intermediate bump blends into the broad focus-point peak. When the uncertainties in m_t and m_b are set to 0, we obtain a narrow peak in the focus-point region.

Using the fully normalized likelihood function \mathcal{L}_{tot} obtained by combining both signs of μ for each value of $\tan\beta$, we can determine the regions in the $(m_{1/2}, m_0)$ planes which correspond to specific CLs. Fig. 7 extends the previous analysis to the entire $(m_{1/2}, m_0)$ plane for $\tan\beta = 10$ and $A_0 = 0$, including both signs of μ . The darkest (blue), intermediate (red) and lightest (green) shaded regions are, respectively, those where the likelihood is above 68%, above 90%, and above 95%. Overall, the likelihood for $\mu < 0$ is less than that for $\mu > 0$ due to the Higgs and $b \rightarrow s\gamma$ constraints. Only the bulk and coannihilation-tail regions appear above the 68% level, but the focus-point region appears above the 90% level, and so cannot be excluded.

The bulk region is more apparent in the right panel of Fig. 7 for $\mu > 0$ than it would be if the experimental error in m_t and the theoretical error in m_h were neglected. Fig. 8 complements the previous figures by showing the likelihood functions as they would appear if there were no uncertainty in

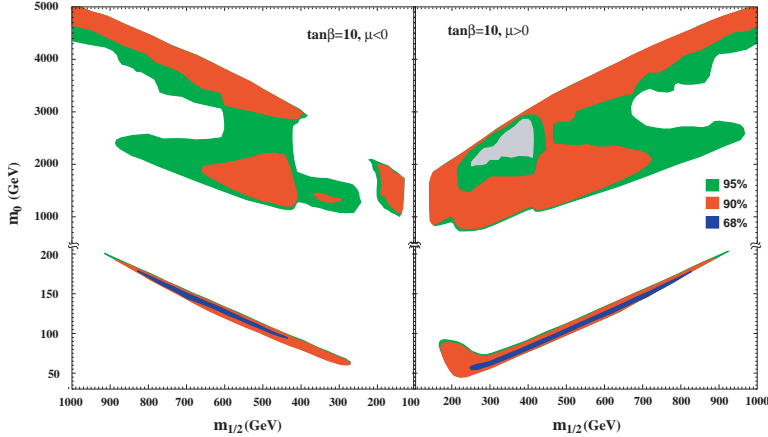


Fig. 7. *Contours of the likelihood at the 68%, 90% and 95% levels for $\tan \beta = 10$, $A_0 = 0$ and $\mu > 0$ (left panel) or $\mu < 0$ (right panel), calculated using information of m_h , $b \rightarrow s\gamma$ and $\Omega_{CDM}h^2$ and the current uncertainties in m_t and m_b .*

m_t , keeping the other inputs the same. We see that, in this case, both the coannihilation and focus-point strips rise above the 68% CL.

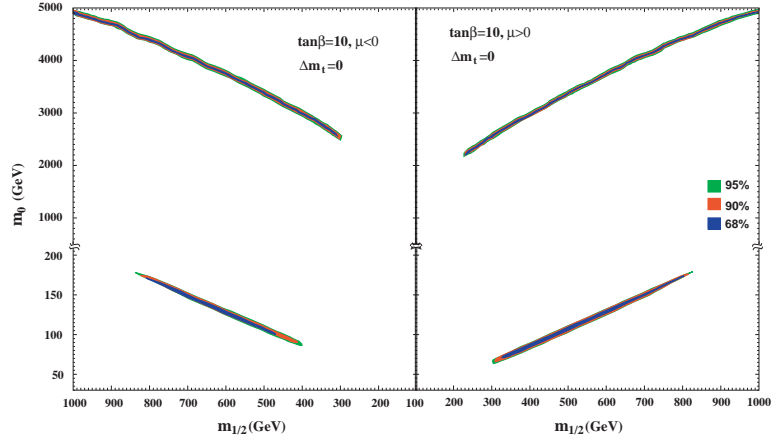


Fig. 8. *As in Fig. 7 but assuming zero uncertainty in m_t .*

Fig. 9 shows the likelihood projection for $\tan \beta = 50$, $A_0 = 0$ and $\mu > 0$. In this case, regions at small $m_{1/2}$ and m_0 are disfavoured by the $b \rightarrow s\gamma$ constraint. The coannihilation region is broadened by a merger with the rapid-annihilation funnel. Both the coannihilation and the focus-point regions

feature strips allowed at the 68% CL, and these are linked by a bridge at the 95% CL.

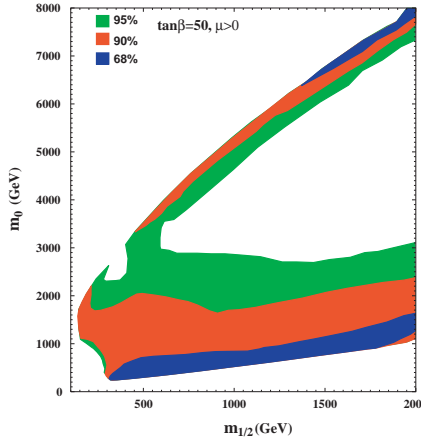


Fig. 9. Likelihood contours as in Fig. 7, but for $\tan\beta = 50$, $A_0 = 0$ and $\mu > 0$.

4 Beyond the CMSSM

The results of the CMSSM described in the previous sections are based heavily on the assumptions of universality of the supersymmetry breaking parameters. One of the simplest generalizations of this model relaxes the assumption of universality of the Higgs soft masses and is known as the NUHM [29]. In this case, the input parameters include μ and m_A , in addition to the standard CMSSM inputs. In order to switch μ and m_A from outputs to inputs, the two soft Higgs masses, m_1, m_2 can no longer be set equal to m_0 and instead are calculated from the electroweak symmetry breaking conditions. The NUHM parameter space was recently analyzed [29] and a sample of the results are shown in Fig. 10.

In the left panel of Fig. 10, we see a $m_{1/2}, m_0$ plane with a relative low value of μ . In this case, an allowed region is found when the LSP contains a non-negligible Higgsino component which moderates the relic density independent of m_0 . To the right of this region, the relic density is too small. In the right panel, we see an example of the m_A, μ plane. The crosses correspond to CMSSM points. In this single pane, we see examples of acceptable cosmological regions corresponding to the bulk region, co-annihilation region and s-channel annihilation through the Higgs pseudo scalar.

Rather than relax the CMSSM, it is in fact possible to further constrain the model. While the CMSSM models described above are certainly

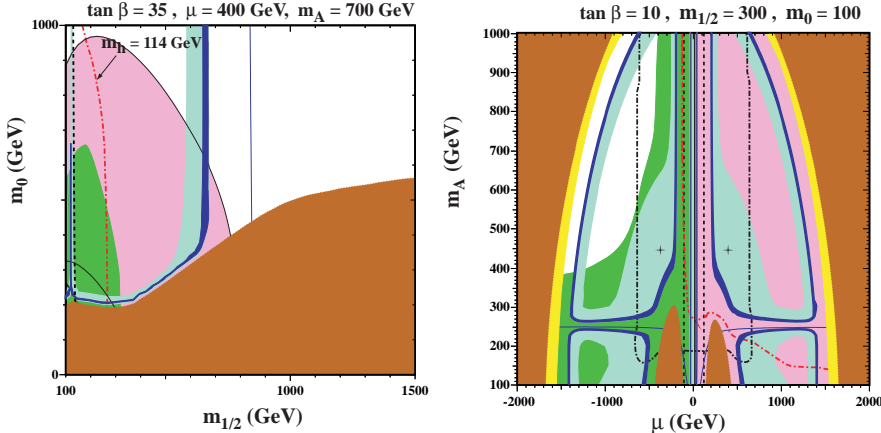


Fig. 10. a) The NUHM ($m_{1/2}, m_0$) plane for $\tan \beta = 35$, (a) $\mu = 400$ GeV and $m_A = 700$ GeV b) the NUHM (μ, m_A) plane for $\tan \beta = 10$, $m_0 = 100$ GeV and $m_{1/2} = 300$ GeV, with $A_0 = 0$. The (red) dot-dashed lines are the contours $m_h = 114$ GeV, and the near-vertical (black) dashed lines are the contours $m_{\chi^\pm} = 103.5$ GeV. The dark (black) dot-dashed lines indicate the GUT stability constraint. Only the areas inside these curves (small μ) are allowed by this constraint. The light (turquoise) shaded areas are the cosmologically preferred regions with $0.1 \leq \Omega_\chi h^2 \leq 0.3$. The darker (blue) portion of this region corresponds to the newer WMAP densities. The dark (brick red) shaded regions is excluded because a charged particle is lighter than the neutralino, and the lighter (yellow) shaded regions is excluded because the LSP is a sneutrino. The medium (green) shaded region is excluded by $b \rightarrow s\gamma$. The regions allowed by the $g - 2$ constraint are shaded (pink) and bounded by solid black lines. The solid (blue) curves correspond to $m_\chi = m_A/2$.

mSUGRA inspired, minimal supergravity models can be argued to be still more predictive. Let us assume that supersymmetry is broken in a hidden sector so that the superpotential can be written as a sum of two terms, $W = F(\phi) + g(\zeta)$, where ϕ represents all observable fields and ζ all hidden sector fields. We furthermore must choose $g(\zeta)$ such that when ζ picks up a vacuum expectation value, supersymmetry is broken. When the potential is expanded and terms inversely proportional to Planck mass are dropped, one finds [30] 1) scalar mass universality with $m_0 = \langle g \rangle$; 2) trilinear mass universality with $A_0 = \langle dg/d\zeta \rangle \langle \zeta \rangle + \langle g \rangle \langle \zeta \rangle^2$; and 3) $B_0 = A_0 - m_0$.

In the simplest version of the theory [31], the universal trilinear soft supersymmetry-breaking terms are $A = (3 - \sqrt{3})m_0$ and bilinear soft supersymmetry-breaking term is $B = (2 - \sqrt{3})m_0$, i.e., a special case of the general relation above between B and A .

Given a relation between B_0 and A_0 , we can no longer use the standard CMSSM boundary conditions, in which $m_{1/2}$, m_0 , A_0 , $\tan \beta$, and $\text{sgn}(\mu)$ are input at the GUT scale with μ and B determined by the electroweak

symmetry breaking condition. Now, one is forced to input B_0 and instead $\tan \beta$ is calculated from the minimization of the Higgs potential [32].

In Fig. 11, the contours of $\tan \beta$ (solid blue lines) in the $(m_{1/2}, m_0)$ planes for two values of $\hat{A} = A_0/m_0$, $\hat{B} = B_0/m_0 = \hat{A} - 1$ and the sign of μ are displayed [32]. Also shown are the contours where $m_{\chi^\pm} > 104$ GeV (near-vertical black dashed lines) and $m_h > 114$ GeV (diagonal red dash-dotted lines). The excluded regions where $m_\chi > m_{\tilde{\tau}_1}$ have dark (red) shading, those excluded by $b \rightarrow s\gamma$ have medium (green) shading, and those where the relic density of neutralinos lies within the WMAP range $0.094 \leq \Omega_\chi h^2 \leq 0.129$ have light (turquoise) shading. Finally, the regions favoured by $g_\mu - 2$ at the 2- σ level are medium (pink) shaded.

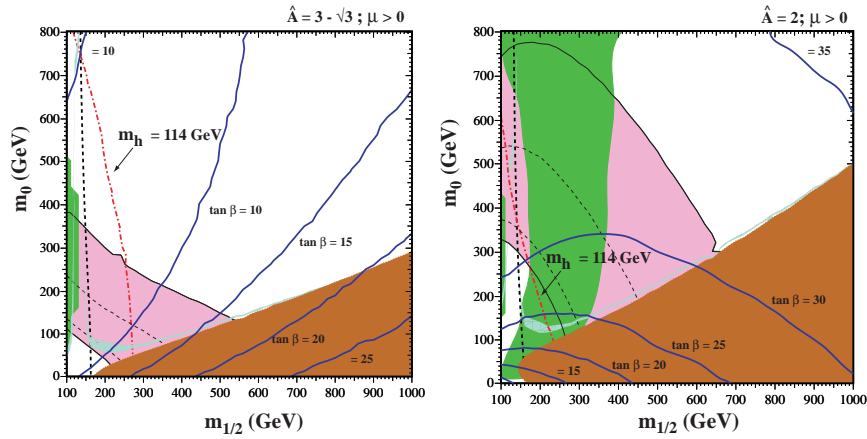


Fig. 11. Examples of $(m_{1/2}, m_0)$ planes with contours of $\tan \beta$ superposed, for $\mu > 0$ and (a) the simplest Polonyi model with $\hat{A} = 3 - \sqrt{3}$, $\hat{B} = \hat{A} - 1$ and (b) $\hat{A} = 2.0$, $\hat{B} = \hat{A} - 1$. In each panel, we show the regions excluded by the LEP lower limits on MSSM particles, those ruled out by $b \rightarrow s\gamma$ decay (medium green shading), and those excluded because the LSP would be charged (dark red shading). The region favoured by the WMAP range has light turquoise shading. The region suggested by $g_\mu - 2$ is medium (pink) shaded.

In panel (a) of Fig. 11, we see that the Higgs constraint combined with the relic density requires $\tan \beta \gtrsim 11$, whilst the relic density also enforces $\tan \beta \lesssim 20$. For a given point in the $m_{1/2} - m_0$ plane, the calculated value of $\tan \beta$ increases as \hat{A} increases. This is seen in panel (b) of Fig. 11, when $\hat{A} = 2.0$, close to its maximal value for $\mu > 0$, the $\tan \beta$ contours turn over towards smaller $m_{1/2}$, and only relatively large values $25 \lesssim \tan \beta \lesssim 35$ are allowed by the $b \rightarrow s\gamma$ and $\Omega_{CDM} h^2$ constraints, respectively. For any given value of \hat{A} , there is only a relatively narrow range allowed for $\tan \beta$.

5 Detectability

The question of detectability with respect to supersymmetric models is of key importance particularly with the approaching start of the LHC. As an aid to the assessment of the prospects for detecting sparticles at different accelerators, benchmark sets of supersymmetric parameters have often been found useful, since they provide a focus for concentrated discussion [33, 34, 35]. A set of proposed post-LEP benchmark scenarios [33] were chosen to span the CMSSM. Five of the chosen points are in the ‘bulk’ region at small $m_{1/2}$ and m_0 , four are spread along the coannihilation ‘tail’ at larger $m_{1/2}$ for various values of $\tan\beta$. Two points are in rapid-annihilation ‘funnels’ at large $m_{1/2}$ and m_0 . Two points were chosen in the focus-point region at large m_0 . The proposed points range over the allowed values of $\tan\beta$ between 5 and 50.

In Fig. 12, a comparison of the numbers of different MSSM particles that should be observable at different accelerators in the various benchmark scenarios [35], ordered by their consistency with $g_\mu = 2$. The qualities of the prospective sparticle observations at hadron colliders and linear e^+e^- colliders are often very different, with the latter’s clean experimental environments providing prospects for measurements with better precision. Nevertheless, Fig. 12 already restates the clear message that hadron colliders and linear e^+e^- colliders are largely complementary in the classes of particles that they can see, with the former offering good prospects for strongly-interacting sparticles such as squarks and gluinos, and the latter excelling for weakly-interacting sparticles such as charginos, neutralinos and sleptons.

Clearly the center of mass energy of any future linear collider is paramount towards the supersymmetry discovery potential of the machine. This is seen in Fig. 12 for the benchmark points as more sparticles become observable at higher CM energy. We can emphasize this point in general models by plotting the masses of the two lightest (observable) sparticles in supersymmetric models. For example, in Fig. 13 [36], a scatter plot of the masses of the lightest visible supersymmetric particle (LVSP) and the next-to-lightest visible supersymmetric particle (NLVSP) is shown for the CMSSM. Once again, points selected satisfy all phenomenological constraints. We do not consider the LSP itself to be visible, nor any heavier neutral sparticle that decays invisibly inside the detector, such as $\tilde{\nu} \rightarrow \nu\chi$ when $\tilde{\nu}$ is the next-to-lightest sparticle in a neutralino LSP scenario. The LVSP and the NLVSP are the lightest sparticles likely to be observable in collider experiments.

All points shown in Fig. 13 satisfy the phenomenological constraints discussed above. The dark (red) squares represent those points for which the relic density is outside the WMAP range, and for which all coloured sparticles (squarks and gluinos) are heavier than 2 TeV. The CMSSM parameter reach at the LHC has been analyzed in [37]. To within a few percent accuracy, the CMSSM reach contours presented in [37] coincide with the 2-TeV contour for the lightest squark (generally the stop) or gluino, so we regard

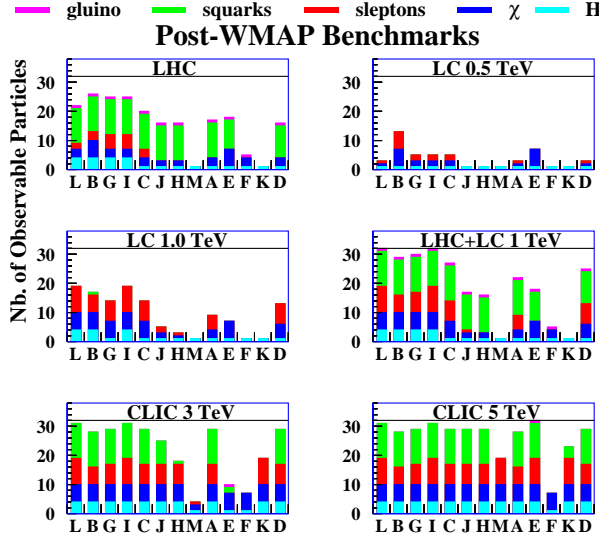


Fig. 12. Summary of the numbers of MSSM particles that may be detectable at various accelerators in the updated benchmark scenarios. We see that the capabilities of the LHC and of linear e^+e^- colliders are largely complementary. We re-emphasize that mass and coupling measurements at e^+e^- colliders are usually much cleaner and more precise than at hadron-hadron colliders such as the LHC, where, for example, it is not known how to distinguish the light squark flavours.

the dark (red) points as unobservable at the LHC. Most of these points have $m_{NLVSP} \gtrsim 1.2$ TeV. Conversely, the medium-shaded (green) crosses represent points where at least one squark or gluino has a mass less than 2 TeV and should be observable at the LHC. The spread of the dark (red) squares and medium-shaded (green) crosses, by as much as 500 GeV or more in some cases, reflects the maximum mass splitting between the LVSP and the NLVSP that is induced in the CMSSM via renormalization effects on the input mass parameters. The amount of this spread also reflects our cutoff $|A_0| < 1$ TeV, which controls the mass splitting of the third generation sfermions.

The darker (blue) triangles are those points respecting the cosmological cold dark matter constraint. Comparing with the regions populated by dark (red) squares and medium-shaded (green) crosses, one can see which of these models would be detectable at the LHC, according to the criterion in the previous paragraph. We see immediately that the dark matter constraint restricts the LVSP masses to be less than about 1250 GeV and NLVSP masses to be less than about 1500 GeV. In most cases, the identity of the LVSP is the lighter $\tilde{\tau}$. While pair-production of the LVSP would sometimes require a

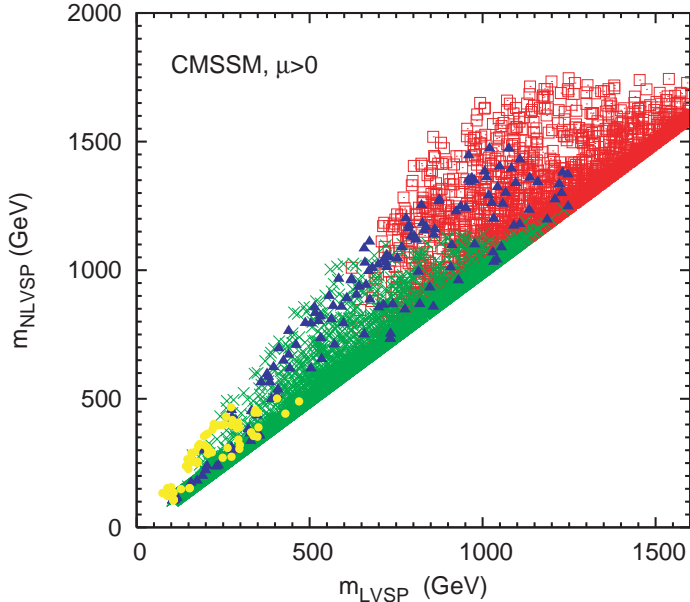


Fig. 13. Scatter plots of the masses of the lightest visible supersymmetric particle (LVSP) and the next-to-lightest visible supersymmetric particle (NLVSP) in the CMSSM for $\mu > 0$. The darker (blue) triangles satisfy all the laboratory, astrophysical and cosmological constraints. For comparison, the dark (red) squares and medium-shaded (green) crosses respect the laboratory constraints, but not those imposed by astrophysics and cosmology. In addition, the (green) crosses represent models which are expected to be visible at the LHC. The very light (yellow) points are those for which direct detection of supersymmetric dark matter might be possible.

CM energy of about 2.5 TeV, in some cases there is a lower supersymmetric threshold due to the associated production of the LSP χ with the next lightest neutralino χ_2 [38]. Examining the masses and identities of the sparticle spectrum at these points, we find that $E_{CM} \gtrsim 2.2$ TeV would be sufficient to see at least one sparticle, as shown in Table 1. Similarly, only a LC with $E_{CM} \geq 2.5$ TeV would be ‘guaranteed’ to see two visible sparticles (in addition to the χ LSP), somewhat lower than the 3.0 TeV one might obtain by requiring the pair production of the NLVSP. Points with $m_{LVSP} \gtrsim 700$ GeV are predominantly due to rapid annihilation via direct-channel H, A poles, while points with $200 \text{ GeV} \lesssim m_{LVSP} \lesssim 700$ GeV are largely due to χ -slepton coannihilation.

An $E_{CM} = 500$ GeV LC would be able to explore the ‘bulk’ region at low $(m_{1/2}, m_0)$, which is represented by the small cluster of points around $m_{LVSP} \sim 200$ GeV. It should also be noted that there are a few points with $m_{LVSP} \sim 100$ GeV which are due to rapid annihilation via the light Higgs pole. These points all have very large values of m_0 which relaxes the

Table 1. Centre-of-mass energy (in TeV) required to observe one or two sparticles at a future LC in the CMSSM and NUHM.

Model	$sgn(\mu)$	one sparticle	two sparticles
CMSSM	$\mu > 0$	2.2	2.6
	$\mu < 0$	2.2	2.5
NUHM	$\mu > 0$	2.4	2.8
	$\mu < 0$	2.6	2.9

Higgs mass and chargino mass constraints, particularly when $m_t = 178$ GeV. A LC with $E_{CM} = 1000$ GeV would be able to reach some way into the coannihilation ‘tail’, but would not cover all the WMAP-compatible dark (blue) triangles. Indeed, about a third of these points are even beyond the reach of the LHC in this model. Finally, the light (yellow) filled circles are points for which the elastic χ - p scattering cross section is larger than 10^{-8} pb.

Because the LSP as dark matter is present locally, there are many avenues for pursuing dark matter detection. Direct detection techniques rely on an ample neutralino-nucleon scattering cross-section. The prospects for direct detection for the benchmark points discussed above [39] are shown in Fig. 14. This figure shows rates for the elastic spin-independent and spin dependent scattering cross sections of supersymmetric relics on protons. Indirect searches for supersymmetric dark matter via the products of annihilations in the galactic halo or inside the Sun also have prospects in some of the benchmark scenarios [39].

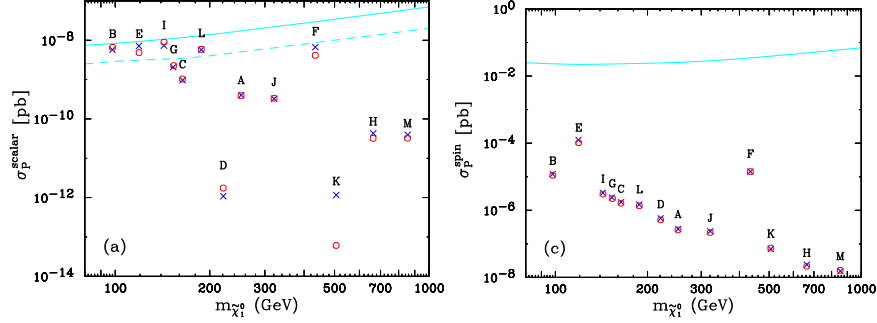


Fig. 14. Elastic cross sections for (a) spin-independent scattering and (b) spin-dependent scattering on protons. Our predictions (blue crosses) are compared with those of **Neutdriver** [40] (red circles) for neutralino-nucleon scattering. Projected sensitivities (a) for **CDMS II** [41] and **CRESST** [42] (solid) and **GENIUS** [43] (dashed) and (b) for a 100 kg **NAIAD** array [44] are also shown.

In Fig. 15, we display the allowed ranges of the spin-independent cross sections in the NUHM when we sample randomly $\tan\beta$ as well as the other NUHM parameters [45]. The raggedness of the boundaries of the shaded regions reflects the finite sample size. The dark shaded regions includes all sample points after the constraints discussed above (including the relic density constraint) have been applied. In a random sample, one often hits points which are perfectly acceptable at low energy scales but when the parameters are run to high energies approaching the GUT scale, one or several of the sparticles mass squared runs negative [46]. This has been referred to as the GUT constraint here. The medium shaded region embodies those points after the GUT constraint has been applied. After incorporating all the cuts, including that motivated by $g_\mu - 2$, we find that the light shaded region where the scalar cross section has the range $10^{-6} \text{ pb} \gtrsim \sigma_{SI} \gtrsim 10^{-10} \text{ pb}$, with somewhat larger (smaller) values being possible in exceptional cases. If the $g_\mu - 2$ cut is removed, the upper limits on the cross sections are unchanged, but much lower values become possible: $\sigma_{SI} \ll 10^{-13} \text{ pb}$. The effect of the GUT constraint on more general supersymmetric models was discussed in [47].

The results from this analysis [45] for the scattering cross section in the NUHM (which by definition includes all CMSSM results) are compared with the previous CDMS [48] and Edelweiss [49] bounds as well as the recent CDMSII results [50] in Fig. 15. While previous experimental sensitivities were not strong enough to probe predictions of the NUHM, the current CDMSII bound has begun to exclude realistic models and it is expected that these bounds improve by a factor of about 20.

This work was partially supported by DOE grant DE-FG02-94ER-40823.

References

1. H. Goldberg, *Phys. Rev. Lett.* **50**, 1419 (1983); J. Ellis, J.S. Hagelin, D.V. Nanopoulos, K.A. Olive and M. Srednicki, *Nucl. Phys.* **B238**, 453 (1984).
2. L.E. Ibanez, *Phys. Lett.* **137B**, 160 (1984); J. Hagelin, G.L. Kane, and S. Raby, *Nucl. Phys.* **B241**, 638 (1984); T. Falk, K. A. Olive and M. Srednicki, *Phys. Lett. B* **339**, 248 (1994).
3. S. Ahlen, et. al., *Phys. Lett.* **B195**, 603 (1987);
D.D. Caldwell, et. al., *Phys. Rev. Lett.* **61**, 510 (1988);
M. Beck et al., *Phys. Lett.* **B336** 141 (1994).
4. see e.g. K.A. Olive and M. Srednicki, *Phys. Lett.* **205B**, 553 (1988);
N. Sato et al. *Phys. Rev.* **D44**, 2220 (1991).
5. J. Ellis, T. Falk, and K.A. Olive, *Phys. Lett.* **B444** (1998) 367 [arXiv:hep-ph/9810360]; J. Ellis, T. Falk, K.A. Olive, and M. Srednicki, *Astr. Part. Phys.* **13** (2000) 181 [Erratum-ibid. **15** (2001) 413] [arXiv:hep-ph/9905481].
6. J. L. Feng, S. Su and F. Takayama, arXiv:hep-ph/0404231; arXiv:hep-ph/0404198; J. L. Feng, A. Rajaraman and F. Takayama, *Phys. Rev. Lett.* **91** (2003) 011302 [arXiv:hep-ph/0302215]; J. R. Ellis, K. A. Olive, Y. Santoso and V. C. Spanos, *Phys. Lett. B* **588** (2004) 7 [arXiv:hep-ph/0312262]; L. Roszkowski and R. Ruiz de Austri, arXiv:hep-ph/0408227.

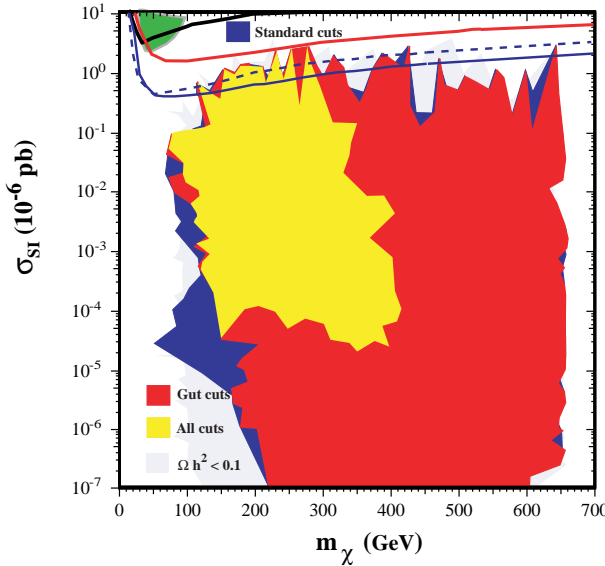


Fig. 15. Ranges of the spin-independent cross section in the NUHM. The ranges allowed by the cuts on $\Omega_\chi h^2$, m_h and $b \rightarrow s\gamma$ have dark shading, those still allowed by the GUT stability cut have medium shading, and those still allowed after applying all the cuts including $g_\mu - 2$ have light shading. The pale shaded region corresponds to the extra area of points with low relic densities, whose cross sections have been rescaled appropriately. Also shown are the limits from the CDMS[48] and Edelweiss[49] experiments as well as the recent CDMSII result [50] on the neutralino-proton elastic scattering cross section as a function of the neutralino mass. The CDMSII limit is stronger than the Edelweiss limit which is stronger than the previous CDMS limit at higher m_χ . The result reported by DAMA [51] is found in the upper left.

7. Joint LEP 2 Supersymmetry Working Group, *Combined LEP Chargino Results, up to 208 GeV*, http://lepsusy.web.cern.ch/lepsusy/www/inos_moriond01/charginos_pub.html.
8. Joint LEP 2 Supersymmetry Working Group, *Combined LEP Selec-tron/Smuon/Stau Results, 183-208 GeV*, http://lepsusy.web.cern.ch/lepsusy/www/sleptons_summer02/slep_2002.html.
9. LEP Higgs Working Group for Higgs boson searches, OPAL Collaboration, ALEPH Collaboration, DELPHI Collaboration and L3 Collaboration, Phys. Lett. B **565** (2003) 61 [arXiv:hep-ex/0306033]. *Searches for the neutral Higgs bosons of the MSSM: Preliminary combined results using LEP data collected at energies up to 209 GeV*, LHWG-NOTE-2001-04, ALEPH-2001-057, DELPHI-2001-114, L3-NOTE-2700, OPAL-TN-699, arXiv:hep-ex/0107030; LHWG Note/2002-01, http://lephiggs.web.cern.ch/LEPHIGGS/papers/July2002_SM/index.html.

10. S. Heinemeyer, W. Hollik and G. Weiglein, *Comput. Phys. Commun.* **124** (2000) 76 [arXiv:hep-ph/9812320]; S. Heinemeyer, W. Hollik and G. Weiglein, *Eur. Phys. J. C* **9** (1999) 343 [arXiv:hep-ph/9812472].
11. S. Chen *et al.* [CLEO Collaboration], *Phys. Rev. Lett.* **87** (2001) 251807 [arXiv:hep-ex/0108032]; BELLE Collaboration, BELLE-CONF-0135. See also K. Abe *et al.* [Belle Collaboration], *Phys. Lett. B* **511** (2001) 151 [arXiv:hep-ex/0103042]; B. Aubert *et al.* [BaBar Collaboration], arXiv:hep-ex/0207076.
12. C. Degrassi, P. Gambino and G. F. Giudice, *JHEP* **0012** (2000) 009 [arXiv:hep-ph/0009337], as implemented by P. Gambino and G. Ganis.
13. M. Carena, D. Garcia, U. Nierste and C. E. Wagner, *Phys. Lett. B* **499** (2001) 141 [arXiv:hep-ph/0010003]; P. Gambino and M. Misiak, *Nucl. Phys. B* **611** (2001) 338; D. A. Demir and K. A. Olive, *Phys. Rev. D* **65** (2002) 034007 [arXiv:hep-ph/0107329]; T. Hurth, arXiv:hep-ph/0106050; *Rev. Mod. Phys.* **75**, 1159 (2003) [arXiv:hep-ph/0212304].
14. [The Muon g-2 Collaboration], *Phys. Rev. Lett.* **92** (2004) 161802, hep-ex/0401008.
15. M. Davier, S. Eidelman, A. Höcker and Z. Zhang, *Eur. Phys. J. C* **31** (2003) 503, hep-ph/0308213; see also K. Hagiwara, A. Martin, D. Nomura and T. Teubner, *Phys. Rev. D* **69** (2004) 093003, hep-ph/0312250; S. Ghozzi and F. Jegerlehner, *Phys. Lett. B* **583** (2004) 222, hep-ph/0310181; M. Knecht, hep-ph/0307239; K. Melnikov and A. Vainshtein, hep-ph/0312226; J. de Troconiz and F. Yndurain, hep-ph/0402285.
16. C. L. Bennett *et al.*, *Astrophys. J. Suppl.* **148** (2003) 1; D. N. Spergel *et al.*, *Astrophys. J. Suppl.* **148** (2003) 175; H. V. Peiris *et al.*, *Astrophys. J. Suppl.* **148** (2003) 213.
17. J. R. Ellis, K. A. Olive, Y. Santoso and V. C. Spanos, *Phys. Lett. B* **565** (2003) 176 [arXiv:hep-ph/0303043].
18. H. Baer and C. Balazs, *JCAP* **0305** (2003) 006 [arXiv:hep-ph/0303114].
19. A. B. Lahanas and D. V. Nanopoulos, *Phys. Lett. B* **568** (2003) 55 [arXiv:hep-ph/0303130]; U. Chattopadhyay, A. Corsetti and P. Nath, *Phys. Rev. D* **68** (2003) 035005 [arXiv:hep-ph/0303201]; C. Munoz, *Int. J. Mod. Phys. A* **19**, 3093 (2004) [arXiv:hep-ph/0309346]; R. Arnowitt, B. Dutta and B. Hu, arXiv:hep-ph/0310103.
20. M. Drees and M. M. Nojiri, *Phys. Rev. D* **47** (1993) 376; H. Baer and M. Brhlik, *Phys. Rev. D* **53** (1996) 59; and *Phys. Rev. D* **57** (1998) 567; H. Baer, M. Brhlik, M. A. Diaz, J. Ferrandis, P. Mercadante, P. Quintana and X. Tata, *Phys. Rev. D* **63** (2001) 015007; A. B. Lahanas, D. V. Nanopoulos and V. C. Spanos, *Mod. Phys. Lett. A* **16** (2001) 1229.
21. J. R. Ellis, T. Falk, G. Ganis, K. A. Olive and M. Srednicki, *Phys. Lett. B* **510** (2001) 236 [arXiv:hep-ph/0102098].
22. J. L. Feng, K. T. Matchev and T. Moroi, *Phys. Rev. D* **61** (2000) 075005 [arXiv:hep-ph/9909334].
23. A. Romanino and A. Strumia, *Phys. Lett. B* **487** (2000) 165, hep-ph/9912301.
24. J. R. Ellis and K. A. Olive, *Phys. Lett. B* **514** (2001) 114 [arXiv:hep-ph/0105004].
25. W. de Boer, M. Huber, C. Sander and D. I. Kazakov, arXiv:hep-ph/0106311.
26. J. R. Ellis, K. A. Olive, Y. Santoso and V. C. Spanos, *Phys. Rev. D* **69** (2004) 095004 [arXiv:hep-ph/0310356].
27. J. R. Ellis, K. Enqvist, D. V. Nanopoulos and F. Zwirner, *Mod. Phys. Lett. A* **1** (1986) 57; R. Barbieri and G. F. Giudice, *Nucl. Phys. B* **306** (1988) 63.

28. J. R. Ellis, K. A. Olive and Y. Santoso, *New J. Phys.* **4** (2002) 32 [arXiv:hep-ph/0202110].
29. J. Ellis, K. Olive and Y. Santoso, *Phys.Lett.* **B539** (2002) 107 [arXiv:hep-ph/0204192].; J. R. Ellis, T. Falk, K. A. Olive and Y. Santoso, *Nucl. Phys. B* **652** (2003) 259 [arXiv:hep-ph/0210205].
30. For reviews, see: H. P. Nilles, *Phys. Rep.* **110** (1984) 1; A. Brignole, L. E. Ibanez and C. Munoz, arXiv:hep-ph/9707209, published in *Perspectives on supersymmetry*, ed. G. L. Kane, pp. 125-148; H.-P. Nilles, M. Srednicki and D. Wyler, *Phys. Lett.* **120B** (1983) 345; L.J. Hall, J. Lykken and S. Weinberg, *Phys. Rev.* **D27** (1983) 2359.
31. J. Polonyi, Budapest preprint KFKI-1977-93 (1977); R. Barbieri, S. Ferrara and C.A. Savoy, *Phys. Lett.* **119B** (1982) 343.
32. J. R. Ellis, K. A. Olive, Y. Santoso and V. C. Spanos, *Phys. Lett. B* **573** (2003) 162 [arXiv:hep-ph/0305212]; *Phys. Rev. D* **70** (2004) 055005 [arXiv:hep-ph/0405110].
33. M. Battaglia et al., *Eur. Phys. J.* **C 22** (2001) 535, hep-ph/0106204.
34. B. Allanach et al., *Eur. Phys. J.* **C 25** (2002) 113, hep-ph/0202233.
35. M. Battaglia, A. De Roeck, J. Ellis, F. Gianotti, K. Olive and L. Pape, *Eur. Phys. J.* **C 33** (2004) 273, hep-ph/0306219.
36. J. R. Ellis, K. A. Olive, Y. Santoso and V. C. Spanos, arXiv:hep-ph/0408118.
37. H. Baer, C. Balazs, A. Belyaev, T. Krupovnickas and X. Tata, *JHEP* **0306** (2003) 054 [arXiv:hep-ph/0304303].
38. A. Djouadi, M. Drees and J. L. Kneur, *JHEP* **0108** (2001) 055 [arXiv:hep-ph/0107316].
39. J. Ellis, J. L. Feng, A. Ferstl, K. T. Matchev and K. A. Olive, *Eur. Phys. J.* **C24** (2002) 311 [arXiv:astro-ph/0110225].
40. G. Jungman, M. Kamionkowski and K. Griest, *Phys. Rept.* **267**, 195 (1996) [arXiv:hep-ph/9506380]; <http://t8web.lanl.gov/people/jungman/neut-package.html>.
41. CDMS Collaboration, R. W. Schnee et al., *Phys. Rep.* **307** (1998) 283.
42. CRESST Collaboration, M. Bravin et al., *Astropart. Phys.* **12** (1999) 107.
43. H. V. Klapdor-Kleingrothaus, arXiv:hep-ph/0104028.
44. N. J. Spooner et al., *Phys. Lett. B* **473**, 330 (2000).
45. J. R. Ellis, A. Ferstl, K. A. Olive and Y. Santoso, *Phys. Rev. D* **67**, 123502 (2003) [arXiv:hep-ph/0302032].
46. T. Falk, K. A. Olive, L. Roszkowski and M. Srednicki, *Phys. Lett. B* **367** (1996) 183 [arXiv:hep-ph/9510308]; A. Riotto and E. Roulet, *Phys. Lett. B* **377** (1996) 60 [arXiv:hep-ph/9512401]; A. Kusenko, P. Langacker and G. Segre, *Phys. Rev. D* **54** (1996) 5824 [arXiv:hep-ph/9602414]; T. Falk, K. A. Olive, L. Roszkowski, A. Singh and M. Srednicki, *Phys. Lett. B* **396** (1997) 50 [arXiv:hep-ph/9611325].
47. J. R. Ellis, K. A. Olive, Y. Santoso and V. C. Spanos, *Phys. Rev. D* **69**, 015005 (2004) [arXiv:hep-ph/0308075].
48. D. Abrams et al. [CDMS Collaboration], *Phys.Rev.* **D66** (2002) 122003 [arXiv:astro-ph/0203500].
49. A. Benoit et al., *Phys.Lett.* **B545** (2002) 43 [arXiv:astro-ph/0206271].
50. D. S. Akerib et al. [CDMS Collaboration], arXiv:astro-ph/0405033.
51. DAMA Collaboration, R. Bernabei et al., *Phys. Lett.* **B436** (1998) 379.